

JGR Space Physics



RESEARCH ARTICLE

10.1029/2023JA031354

Key Points:

- Multi-level nested-grid thermosphere-ionosphereelectrodynamics general circulation model has been successfully developed with optimized parallelization and used to simulate Tonga volcano eruption
- Gravity waves (GWs) propagate in the nested mesh more efficiently than global mesh, introducing large perturbations in the ionosphere and thermosphere
- The dominant GW in nested grid has a wavelength of ~400 km, period of 10–30 min and phase speed of ~300 m/s, consistent with observations

Supporting Information:

Supporting Information may be found in the online version of this article.

Correspondence to:

H. Wu, haonanw@g.clemson.edu

Citation:

Wu, H., Lu, X., Wang, W., & Liu, H.-L. (2023). Simulation of the propagation and effects of gravity waves generated by Tonga volcano eruption in the thermosphere and ionosphere using nested-grid TIEGCM. *Journal of Geophysical Research: Space Physics*, 128, e2023JA031354. https://doi.org/10.1029/2023JA031354

Received 30 JAN 2023 Accepted 14 APR 2023

Author Contributions:

Conceptualization: Haonan Wu, Xian Lu, Wenbin Wang, Han-Li Liu Data curation: Haonan Wu Formal analysis: Haonan Wu Funding acquisition: Xian Lu

© 2023. The Authors.

This is an open access article under the terms of the Creative Commons Attribution-NonCommercial-NoDerivs License, which permits use and distribution in any medium, provided the original work is properly cited, the use is non-commercial and no modifications or adaptations are made.

Simulation of the Propagation and Effects of Gravity Waves Generated by Tonga Volcano Eruption in the Thermosphere and Ionosphere Using Nested-Grid TIEGCM

Haonan Wu¹, Xian Lu¹, Wenbin Wang², and Han-Li Liu²

¹Department of Physics and Astronomy, Clemson University, Clemson, SC, USA, ²High Altitude Observatory, National Center for Atmospheric Research, Boulder, CO, USA

Abstract The Hunga Tonga-Hunga Ha'apai volcano eruption on 15 January 2022 triggered strong atmospheric gravity wave (GW) activity in the upper atmosphere, which was later detected by various observations. We perform one of the first ionosphere-thermosphere (I-T) model studies of the GW effects from the Tonga eruption in the ionosphere-thermosphereI-T system using the thermosphere-ionosphereelectrodynamics general circulation model (TIEGCM). We implement a high-resolution mesh inside a regional domain (nested grid) in addition to the global low-resolution mesh, which differs from the standard global uniform resolution setup. The nested-grid TIEGCM (TIEGCM-NG) successfully simulates the observed wave propagation and effects in the I-T system by further nudging GW fields at TIEGCM lower boundaries (~97 km) using output from the high-resolution whole atmosphere community climate model with thermosphere and ionosphere extension simulations. The simulation results indicate that the critical parameter to simulate GW propagation is horizontal resolution. Inside the high-resolution nested region, GWs with horizontal wavelengths of ~400 km and periods of 10-30 min can propagate outward and upward and produce significant ionospheric disturbances close to observations. Outside the nested region, only long-wavelength, low-frequency waves survive. Another test indicates that GWs can be better resolved when geopotential height is nudged at TIEGCM lower boundaries. With the capability of simultaneously simulating local, small to mesoscale I-T processes, TIEGCM-NG is superior to global high-resolution simulations due to its largely reduced computation cost and may find its application in the study of I-T system regional dynamics.

Plain Language Summary We develop nested-grid thermosphere-ionosphere-electrodynamics general circulation model (TIEGCM-NG) which is a nested-grid extension of TIEGCM that embeds a high-resolution regional mesh inside a low-resolution global mesh. Computation costs of high-resolution simulations are largely reduced in this way by focusing computing resources only inside the region of interest. We apply this new model to study the gravity wave (GW) effects from the Tonga eruption in the ionosphere-thermosphere (I-T) system. Numerical experiments indicate that the GW generates considerable wind and temperature perturbations in the high-resolution mesh, which suggests that the resolution is essential to the propagation of GWs in the thermosphere. High-resolution model simulations also correctly reproduce the electron density perturbations close to ionospheric observations. The success of TIEGCM-NG stimulates us to further investigate the physical properties of GW propagations in the I-T system.

1. Introduction

Atmospheric gravity waves (GWs) play an important role in energy and momentum coupling from the lower to the upper atmosphere (Fritts, 1984; Fritts & Alexander, 2003). GW sources are manifold, including topography, convection, wind shear, geostrophic adjustment, body forcing, and wave-wave interactions (Fritts & Nastrom, 1992; Nastrom & Fritts, 1992). GWs can propagate to the mesosphere and thermosphere, which leads to changes in the energy and momentum budget (Alexander et al., 2010; Vadas & Fritts, 2005). GW impacts manifest in the ionospheric *E* and *F* regions in the form of traveling ionosphere disturbances (TIDs, Fritts & Lund, 2011; Hines, 1960) or sporadic *E* layers (van Eyken et al., 1982). The upward propagating GWs may dissipate or break and transfer momentum and energy to the mean background winds, making it an efficient way to connect the lower atmosphere source region to the upper atmosphere (Fritts & Alexander, 2003; Holton, 1982; Lindzen, 1981). It is also crucial in numerical models to correctly account for the GW effects to produce

WU ET AL. 1 of 15



Journal of Geophysical Research: Space Physics

10.1029/2023JA031354

Investigation: Haonan Wu, Xian Lu, Wenbin Wang, Han-Li Liu Methodology: Haonan Wu, Xian Lu, Wenbin Wang, Han-Li Liu Project Administration: Xian Lu Resources: Haonan Wu, Xian Lu, Wenbin Wang, Han-Li Liu Software: Haonan Wu Supervision: Xian Lu Validation: Haonan Wu Visualization: Haonan Wu Writing – original draft: Haonan Wu Writing – review & editing: Haonan Wu, Xian Lu, Wenbin Wang, Han-Li Liu

temperature and wind profiles comparable to observations (Holton, 1983; McFarlane, 1987; Palmer et al., 1986; Vadas & Liu, 2009).

On 15 January 2022, a volcano erupted at Hunga Tonga-Hunga Ha'apai (20.5°S, 175.4°W) and produced a vertical plume over 30 km tall with a top above 55 km (Carr et al., 2022). The huge energy release in the initial explosion (10-28EJ) and the subsequent plume triggered atmospheric waves across a wide range of wavelength and frequency. The eruption also ejects a large amount of water vapor (~150 Tg) into the stratosphere, which acts as a secondary wave source in the form of latent heat release as reported by Millán et al. (2022) and Zhu et al. (2022). The generated waves propagated over long distances and were reported worldwide from surface to the ionosphere by satellite and ground-based observations (e.g., Wright et al., 2022). Large neutral wind variations were captured by the Michelson Interferometer for Global High-resolution Thermospheric Imaging onboard the Ionospheric Connection Explorer (ICON), causing the equatorial electroiet to switch directions from eastward to westward (Harding et al., 2022). The GW activity due to the eruption was recorded by the Sounding of the Atmosphere using Broadband Emission Radiometry as temperature variations were enhanced by a factor of 1.5 compared to the days before and after the eruption (X. Liu et al., 2022). Ern et al. (2022) analyzed the temperature profiles from the Atmospheric Infrared Sounder and the Microwave Limb Sounder and found strong mesoscale GW signals. They performed a ray tracing experiment using the Modern-Era Retrospective analysis for Research and Applications, Version 2 as background atmosphere, and the ray tracing results showed the source was in the vicinity of the volcano which suggests that the GW activities were strongly correlated to the volcano eruption.

There was a moderate geomagnetic storm (Kp = 5.7) the day before the eruption (14 January 2022), and the geomagnetic field impacts from the volcano eruption were examined by Schnepf et al. (2022) and Yamazaki et al. (2022). Concentric ring structures of differential total electron content (TEC) clearly indicating the impact from the eruption-induced outward propagating GWs were reported by Themens et al. (2022) and S.-R. Zhang et al. (2022). The geomagnetic conjugate effects of the ionospheric perturbations caused by the volcano triggered GWs were reported by Lin et al. (2022). Aa et al. (2022) pointed out that the depletion of local TEC measurements could reach as high as 10–15 TEC Unit (TECU). Volcano effects manifested in the range-time-intensity plots of the Super Dual Auroral Radar Network observations as rapid oscillations in the line-of-sight Doppler velocities (J. Zhang et al., 2022). In situ ion density and drift measurements from the Ion Velocity Meter onboard ICON also showed clear signatures of GW impacts (Gasque et al., 2022).

Modeling efforts have been conducted to study the interaction between atmospheric acoustic-GWs and tsunamis at the ocean surface (Lynett et al., 2022; Omira et al., 2022). Inchin et al. (2022) solved the 3D nonlinear compressible Navier-Stokes equations using atmospheric Model for Acoustic-Gravity wave Interaction and Coupling (MAGIC) and confirmed that tsunami generated acoustic-GWs can directly influence the mesopause airglow. Amores et al. (2022) utilized the Semi-implicit Cross-scale Hydroscience Integrated System Model to study the fast-moving Lamb waves excited by the Tonga volcano eruption and the simulation results agreed well with the arrival time measured by satellite observations.

However, the modeling efforts of GW propagation in the upper atmosphere and its impact on the ionosphere remain sparse. We present here a modeling study of the volcano triggered GWs and their effects in the ionosphere-thermosphere (I-T) system using the thermosphere-ionosphere-electrodynamics general circulation model (TIEGCM) with a nested grid extension. TIEGCM self-consistently solves the continuity, momentum, thermodynamic, and ion transport equations from 97 to ~600 km (Qian et al., 2014). Nested-grid TIEGCM (TIEGCM-NG) is an extension of TIEGCM version 2.0 which solves the same, full set of first-principle equations inside the regional domain. It provides a high-resolution regional description of the I-T system and extends the capability of studying neutral and electro-dynamical processes to mesoscales. The multi-level nesting capability provides an even finer view of the I-T processes and enables the comparative studies with the local high-resolution observations. TIEGCM-NG is also a more computationally efficient tool for studying meso- to small scale I-T processes than the globally high-resolution model. In this study, we further add the nudging capability, which is an efficient approach in subscribing waves propagating from below.

TIEGCM-NG is inspired by the Thermosphere-Ionosphere Nested Grid Model (TING, Wang et al., 1999), which is a nested-grid extension built upon the thermosphere-ionosphere general circulation model (TIGCM, Roble et al., 1988). TIGCM is the predecessor of TIEGCM, in which electrodynamics were missing. TIEGCM self-consistently solves electrodynamic coupling processes (Richmond et al., 1992), can better simulate the I-T system than TIGCM, and produces output that has better agreement with observations. That leads to

WU ET AL. 2 of 15

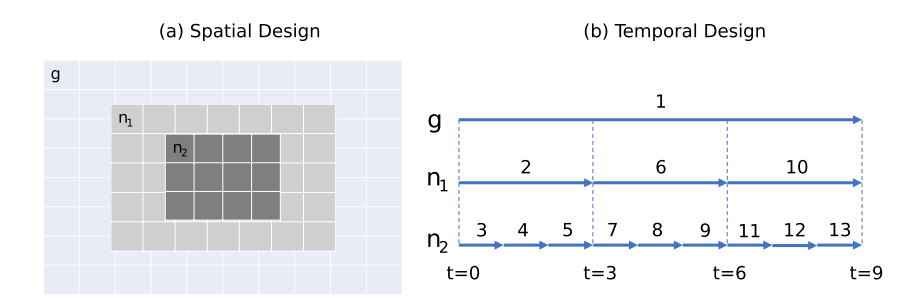


Figure 1. Schematic diagrams showing the (a) spatial and (b) temporal design of a 3-level nested grid. g stands for global, n_1 stands for the first level nested grid, and n_2 stands for the second level nested grid. Numbers in panel (b) represent the workflow of nested-grid thermosphere-ionosphere-electrodynamics general circulation model.

TIEGCM-NG, an updated version of TING with a more complete set of physical processes of self-consistently resolved wind dynamo. TIEGCM-NG also extends the nesting capability to allow for arbitrary nesting levels compared to a maximum of 2 levels in TING.

This paper is organized as follows: Section 2 describes the design of TIEGCM-NG in detail and the setup of control experiments. Section 3 discusses the model results. We conclude this study and briefly discuss the possible application of this new model in Section 4.

2. Model Description and Experiment Design

The design of TIEGCM-NG largely follows the original TIEGCM version 2.0 (Qian et al., 2014; Richmond et al., 1992). The physical equations, the same as those in the global domain, are solved separately in the nested domain. The vertical coordinate system is a log-pressure coordinate,

$$z = \log \frac{p_0}{p} \tag{1}$$

where $p_0 = 5 \times 10^{-5}$ Pa. The lower and upper boundaries are at $z = -7(p = 5e^7 \times 10^{-5} = 0.55$ Pa) and $z = 7(p = 5e^{-7} \times 10^{-5} = 4.55 \times 10^{-8}$ Pa), respectively. The temperature (*T*), zonal and meridional winds (*U* and *V*), and geopotential height (*Z*) consist of the complete set of lower boundary conditions and are chosen to specify the lower boundary fields. The differences and connections between the global and nested grid domains in TIEGCM-NG are highlighted in Section 2.1. The additional functionality (nudging) is described in Section 2.2.

2.1. Design of TIEGCM-NG

The spatial design of TIEGCM-NG is illustrated in Figure 1a, which shows a three-level nesting scheme labeled by g (global), n_1 (first level nested grid) and n_2 (second level nested grid). The nested domain is designed as a rectangular region in latitude and longitude which can be chosen to cover an arbitrary portion of the globe except for the poles. The field mapping between the global and nested domains is achieved by a 2D spatial interpolation which allows for the maximum flexibility of the position of the nested grid. When TIEGCM-NG starts, the nested fields are initialized with the global fields. Then, they iterate without re-initialization from the global fields, which means that the field mapping from the global to the whole nested domain happens only once per model run at the model first time step. The lateral boundary conditions of the nested grid domain are chosen to be the time dependent Dirichlet condition, that is, the fields at the boundary are pre-obtained from the global domain at every nested grid time step. The time dependence of the boundary condition is to guarantee the maximum resemblance of the global and nested fields. The information exchange between the global and nested domains follows different procedures from outside inward (global to nested) and from inside outward (nested to global):

- 1. To pass information from the global into the nested domain (inward), boundary mapping is performed. The global fields are extracted and interpolated to the nested grid boundaries at every nested grid time step to be used as the lateral boundary conditions of the nested domain.
- 2. To pass information from the nested to the global domain (outward), direct field mapping is performed. At every global time step, the global fields inside the nested domain are replaced by the nested fields interpolated onto the global grids. Outside the nested domain, the global fields remain untouched.

WU ET AL. 3 of 15

In terms of the horizontal finite difference scheme, instead of using a 4-point centered finite difference (fourth order accuracy) uniformly in the global domain, a 2-point centered difference (second order accuracy) is used at the lateral boundary while a 4-point centered difference is used internally in the nested grid domain. Numerical tests show that resulting numerical noise is minimal (not shown here). The boundary reflection problem, sometimes present in the GW vertical propagation near the upper boundary (e.g., Klemp & Durran, 1983), does not show up in the GW horizontal propagation close to the nested grid lateral boundary in this study.

Due to the decreased grid sizes in the nested domains compared to the global domain, it is desirable to correspondingly decrease the time step in order to retain numerical stability. Sub-cycling in time is used to achieve numerical stability in the nested domain. The time integration of TIEGCM-NG is illustrated in Figure 1b. A 3-level nesting scheme with a 3-step sub-cycling is used to demonstrate the advancing procedure. The numbers in Figure 1b marks the proceeding sequence in each domain. The details in each step are as follows:

- 1. The time iteration starts from the global domain. Within one iteration (time step), the global domain first advances from t = 0 to t = 9. The first level boundaries are extracted from the global field at these two timestamps (t = 0 and t = 9), and they are temporally interpolated to every sub-cycle (t = 3 and t = 6) for iteration.
- 2. Then the first level is advanced from t = 0 to t = 3. By repeating the inward boundary mapping procedure from the global domain to the first level, the second level nested grid boundaries are extracted from the first level at t = 0 and t = 3. Again, the second level lateral boundary conditions are interpolated in time at the second level sub-cycle (t = 1 and t = 2).
- 3. After that, the second level is advanced from t = 0 to t = 1.
- 4. Since there are no higher-level nested domains, the second level is then advanced from t = 1 to t = 2.
- 5. Again, the second level is advanced from t = 2 to t = 3. Now it is the end of the second level iteration, and an outward field mapping happens from the second level to the first level. At t = 3, the first level fields inside the second level nested domain are replaced by the second level fields.
- 6. Then, the first level iterates from t = 3 to t = 6 (steps 6–9) and from t = 6 to t = 9 (steps 10–13), which are repetitions of what has happened from t = 0 to t = 3. Then at t = 9 after the first level fields are updated by the second level, they are further mapped back to the global domain to update the global fields. This finishes the iteration.

Such time iteration is repeated for the next cycle (t = 9 to t = 18) and the model is advanced.

Besides the differences in the spatial setup and time integration highlighted above, another difference between the global and the nested domain is the low latitude electric fields, which are directly obtained from the interpolation of the global electric fields from the global grid instead of solving the electro-dynamo equation in the nested domain. In the other word, the electric fields in the global domain, derived from the global electro-dynamo equation, are used as an additional input to the nested domain.

From the perspective of computation efficiency, TING is generally slow due to its serial programming design, which is not suitable for the current multi-processor computers. TIEGCM-NG is fully parallelized to better use the available computation resources and runs much faster than TING. The efficiency of TIEGCM-NG is tested through a series of different numbers of nested grid points and core processors. The profiling of the parallel implementation indicates that the time cost grows linearly with the nested grid number and the additional time spent on parallelism is minimal.

TIEGCM-NG also leads to a great improvement in the computation efficiency as compared to the globally uniform high-resolution TIEGCM. To perform a run with the highest resolution of 1°, TIEGCM-NG can be faster as much as three times based on a 20-core machine. For higher resolution runs, even more time is saved by utilizing multi-level nesting. The reduction of computation cost is substantial and it becomes affordable to perform high resolution TIEGCM-NG runs on workstations.

2.2. Nudging of the WACCM-X Fields

To study the propagation of GWs originating from the lower atmosphere in TIEGCM-NG, certain wave sources need to be subscribed at the lower boundary. However, due to the sparse observations near the lower boundary altitude (pressure level z = -7, ~97 km), it is nearly impossible to provide self-consistent high-resolution lower boundary conditions from current observations. Here, we resort to numerical results from other models that can provide fields at z = -7. The simulation results from the whole atmosphere community climate model with thermosphere and ionosphere extension (WACCM-X) are used as the lower boundary input for TIEGCM-NG. WACCM-X self-consistently resolves the atmospheric processes from ground to the upper thermosphere (H.-L.

WU ET AL. 4 of 15

21699402, 2023, 4, Downloaded from https

om/doi/10.1029/2023JA031354 by Xian Lu , Wiley Online Library on [03/05/2023]. See the Terms

Liu et al., 2010, 2018; J. Liu et al., 2018). In this study, a high-resolution WACCM-X Spectral Element (SE) run at 0.25° horizontal resolution and 0.1 scale height vertical resolution is used (H.-L. Liu et al., 2022). The new SE dynamical core eliminates the polar singularity of the Finite Volume core used in previous versions of WACCM-X and enables much higher resolutions than it would achieve in the past. High-resolution model simulations fully embrace resolved GW generations, which are typically parameterized in low-resolution runs (Gettelman et al., 2019). For the 15 January 2022 volcano eruption at Hunga Tonga-Hunga Ha'apai, a large surface pressure perturbation is introduced at 04:35 UT (the reported time of eruption) to approximate the effect of the volcano eruption in the model. The magnitude of the perturbation is adjusted to match available pressure observations in other locations. The pressure disturbance induced GWs are soon reflected in other fields and grow in amplitude vertically, leading to large variations at the lower thermosphere. It should be noted that a large amount of water vapor was emitted into the stratosphere during the volcano eruption. The corresponding release of latent heat acts as another source of GWs (Millán et al., 2022; Zhu et al., 2022). However, this secondary GW (generated by latent heat release) is not considered in this study. The only type of GWs to be studied in this paper is the one excited by the initial pressure pulse. WACCM-X outputs diagnostic fields at a frequency of 1 min.

The WACCM-X fields T, U, V, and Z are extracted at $z = -7(p = 0.55 \text{ Pa}, \sim 97 \text{ km})$ to be used as the lower boundary of TIEGCM-NG. In addition, to better resolve the wave propagation near the lower boundary of TIEGCM-NG, another 2 scale heights of the WACCM-X fields are nudged into TIEGCM-NG, up to z = -5 ($p = 5e^5 \times 10^{-5} = 0.07 \text{ Pa}, \sim 110 \text{ km}$). To apply WACCM-X simulation results in TIEGCM-NG, a spatial 3D interpolation is applied to convert from WACCM-X longitude-latitude-z grids to TIEGCM-NG grids. To accommodate for the difference in TIEGCM-NG time steps and the WACCM-X output frequency, temporal interpolation is applied so that TIEGCM-NG is forced by WACCM-X fields at the lower pressure levels at each time step.

The coupling function used to nudge TIEGCM-NG with WACCM-X fields is

$$f_{\text{TIEGCM-NG}} \leftarrow f_{\text{TIEGCM-NG}} + r(f_{\text{WACCM-X}} - f_{\text{TIEGCM-NG}})$$
 (2)

where f is either T, U, V, or Z. As mentioned above, such a replacement is applied at every time step at TIEGCM-NG lower pressure level grids to reflect the driven state by WACCM-X. r is a vertical relaxation factor, which is chosen to decrease exponentially from r = 1 at z = -7 to $r = 10^{-4}$ at z = -5 to allow for a smooth transition from strong constraints near the lower boundary to weak constraints above. The nudging procedure follows the same idea as Maute et al. (2015) and Jones et al. (2018) except for a different altitude range.

In summary, we develop TIEGCM-NG with a nudging capability to study the GW propagation in the I-T system and applied the TIEGCM-NG to simulate the I-T response to the Tonga eruption. In this study, a global 2.5° resolution is used with a single level nested domain of 60°S–20°N, 140°E–230°E(=130°W) at 1° resolution. This domain is chosen to include Tonga (21°S, 175°W) at the nested grid center and have a sufficient horizontal span (40° on each side) to simulate the wave propagation. The vertical resolution in the global and the nested domains are all set as ¼ scale height. The global domain has a time step of 30 s, and 5 sub-cycles are iterated in the nested domain, indicating a nested grid time step of 6s. Diagnostic outputs are saved every minute both in the global and nested domains. Nudging of WACCM-X fields is switched on at 04:35 UT when the eruption takes place and the nudging altitude ranges in both the global and the nested domain are 2 scale heights. Two testing groups are performed to study the sensitivities of model resolutions and nudging fields:

- 1. The nesting functionality is switched on and off to study the impact of the model resolution on the simulation of GW propagation.
- 2. To analyze the sensitivity of nudging different fields in wave propagation, runs with nudging different combinations of *T*, *U*, *V*, and *Z*, all with the nesting functionality on, are performed.

To investigate GW impacts, a separate type of runs (control runs) without nudging lower-boundary GWs is performed to present the undisturbed states and the simulation results in all testing runs are subtracted by their corresponding control runs to represent the effects caused by the nudged GWs. Unless otherwise notified, all the figures shown in this paper are the deviations from the undisturbed states (difference fields).

3. Model Results in GW Propagation

Two groups of runs are performed separately. The first group nudges all four fields (T, U, V, and Z) and differs by whether the nesting functionality is on. This run group mainly studies the importance of resolution in simulating the propagation of waves (Section 3.1). The model runs in the second group are all nested, but the nudged fields

WU ET AL. 5 of 15

21699402, 2023, 4, Downloaded from https://agupubs.onlinelibrary.wiey.com/doi/10.1029/2023JA031354 by Xian Lu , Wiley Online Library on [03/05/2023]. See the Terms and Conditions (https://onlinelibrary.wiley.com/

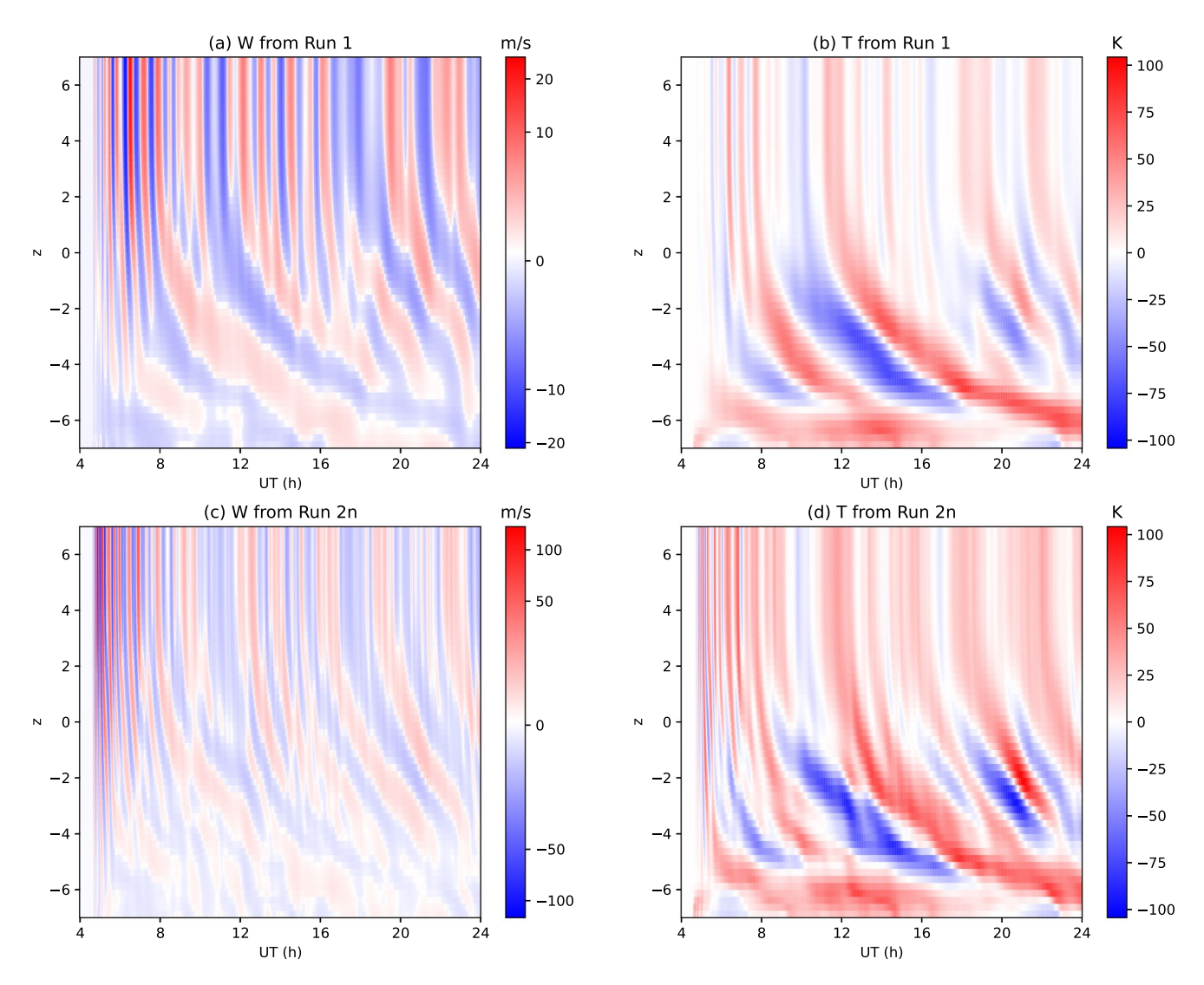


Figure 2. Time-altitude cross sections of vertical wind and temperature perturbations at (21.25°S, 175°W) in (a, b) Run 1 and at (21°S, 175°W) in (c, d) Run 2n. The color scales are different for vertical winds in panel (a, c).

are changed among different ones. This group focuses on the sensitivity of TIEGCM-NG to the nudged fields (Section 3.2).

3.1. Importance of Model Resolution on Wave Propagation

To simplify the notation for the different runs in this section, the run without nesting is denoted as Run 1 and the one with nesting is denoted as Run 2. Note that Run 2 has two sets of outputs, from global and nested domains, therefore they are denoted as Run 2g and Run 2n, respectively.

Figure 2 shows the comparison of the time-altitude profiles of vertical wind and temperature perturbations between Runs 1 and 2n. Figures 2a and 2b show the difference fields at 21.25° S, 175° W (close to the epicenter) in Run 1, and Figures 2c and 2d show those at 21° S, 175° W in Run 2n. The fields in Run 2g are nearly the same as in Run 2n due to interpolation and are therefore omitted. The wave signatures are present at high altitudes in both runs, but the wave amplitude of the vertical wind is significantly larger in Run 2n than in Run 1, over 100 m/s compared to less than 30 m/s (Figures 2a and 2c, color scales are different in Figures 2a and 2c). Both Figures 2b and 2d show downward phase progression below z = 0 of similar amplitude in temperature perturbations ($\sim 100 \text{ K}$), and the periods at these altitudes are generally long (> 8 hr), indicating upward propagating tides or inertial GWs of similar magnitude. Above z = 0, the vertical wavelengths become large due to increased diffusivity and ion drag, while nested results tend to show higher-frequency perturbations (< 1 hr) than Run 1.

WU ET AL. 6 of 15

As shown in Figures 2a and 2c, the vertical propagating wave shifts toward shorter periods at higher altitudes, and wave periods are shorter at these altitudes in Figure 2c compared to Figure 2a. Figure 3 shows the vertical wind wave spectra from 05:00 to 08:00 UT at different altitudes in Runs 1 and 2n. Here, the vertical wind itself is plotted (not the difference field). The direct component is marked as the infinite period in the figure. At the lowest altitude (z = -7), there are no significant wave components shorter than 15 min and long period components dominate, especially for the temporal mean (direct component). At high altitudes in Run 1, the wave periods range from 15 to 45 min centered around 40 min, and no shorter period signals than 12 min are observed. However, in Run 2n, the period components below 40 min grow in altitude and eventually the wave spectra are excited in a broad band from 5 to 45 min at high altitudes. Also, different from the dominant 40 min period in Run 1, three spectral peaks at 40 min, 20 and 12 min arise with a similar magnitude. The change of the dominant wave period with altitude is likely associated with the filtering effect of background winds (Alexander et al., 2010; Fritts & Alexander, 2003).

The amplitude growth of waves with altitudes can cause significant perturbations in the upper thermosphere. Figure 4 shows the horizontal structures of vertical wind and temperature perturbations at 08:00 UT, z=2 (~320 km) in Runs 1 and 2. Figures 4a and 4b are from Run 1; Figures 4c and 4d are from Run 2g overlaid by Run 2n inside the boxed region. The geopotential height and temperature (not the perturbation field) from WACCM-X are extracted at the TIEGCM lower boundary (z=-7) and plotted in Figures 4e and 4f for comparison. Comparing Figures 4d and 4f, the concentric ring patterns are clear at both lower boundary and upper thermosphere (also seen in Figures 4c and 4e) indicating the upward propagation of GWs. However, the differences between Figures 4a and 4c (Figures 4b and 4d) are remarkable. The wave components of short wavelengths (~4° ≈ 400 km) dominate the nested domain while in the global run with no nesting, only waves with much longer wavelengths (~20° ≈ 2,000 km) survive. Also, wave amplitudes in Run 2n are significantly larger than those in Run 1, which indicates that, the shorter wavelengths (~400 km) carry the most wave energy in the wave propagation; but in Run 1, due to the insufficient horizontal resolution (2.5° ≈ 250 km), the wave components below 500 km are dissipative and eventually removed from the wave spectra (Nyquist theorem). To better illustrate the horizontal propagation of GWs, a movie is provided in Supporting Information S1 to show the time evolution of the vertical wind and temperature perturbations.

In terms of traveling atmospheric disturbance (TAD) propagation, time-latitude profiles of vertical wind and temperature perturbations are shown at a constant altitude (z=2) and longitude (175°W) in Figure 5 to demonstrate the horizontal wave propagation. This longitude is chosen to cross the epicenter which represents the path of wave propagation. Both runs show clear latitudinal propagations, but the wave amplitude is significantly larger in Run 2n compared to Run 1; the wave speed is estimated to be $10^{\circ}/h \approx 300$ m/s in both runs, much slower than the local sound speed (typically ~ 800 m/s), indicating that the propagating wave is indeed a GW. No significant difference is found in the wave amplitude or speed along northward and southward directions, which indicates that the wave propagation does not have a preferential direction.

The large GW amplitudes cause significant ionospheric perturbations. Figure 6 shows electron density perturbations at z=2 and differential TEC in both runs. This altitude is close to the ionospheric F_2 peak and is therefore chosen to represent the variations of the ionosphere. Again, the concentric ring structure indicative of outward propagating waves is clear in Figures 6c and 6d, on the order of 10^5 cm⁻³ and 5 TECU, at a similar level as the Global Navigation Satellite System TEC observations (~5 TECU as shown in Figure 2 of Aa et al., 2022). In contrast, though electron density perturbations are present in Run 1, the wave pattern is of a much larger scale and its magnitude is smaller. In both runs, the wave patterns are clearer in the north direction than the south direction because the electron density peaks at a northern equatorial latitude.

The horizontal propagations of ionospheric perturbations are shown in Figure 7. The time-latitude cross sections are shown at the same altitude (z = 2) and longitude (175°W) as in Figure 5. The TID speed is estimated to be 300 m/s, of a similar magnitude as TAD, which indicates that the source of the TIDs is most likely the neutral variation resulting from the volcano eruption. The estimated TID speed is in accordance with the slow mode of the near-field variations in Figure 2 of Themens et al. (2022) and Figure 3 of S.-R. Zhang et al. (2022). Just as shown in Figure 6, the northward propagation of TID (\sim 2 TECU) in Figure 7 is significantly stronger than that in the southward direction (<1 TECU).

WU ET AL. 7 of 15

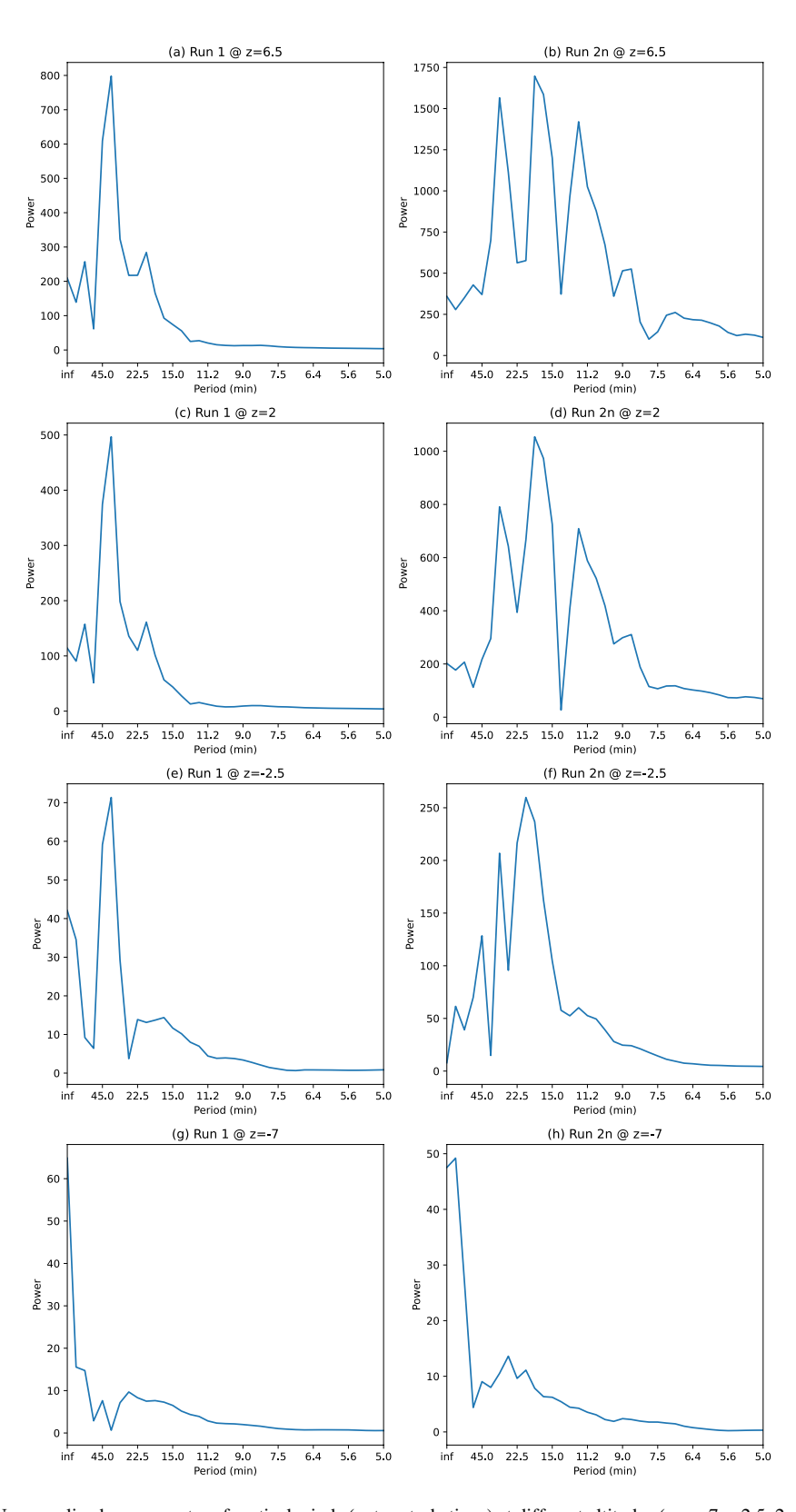


Figure 3. Unnormalized wave spectra of vertical winds (not perturbations) at different altitudes (z = -7, -2.5, 2, 6.5) in (a, c, e, and g) Runs 1 and (b, d, f, and h) 2n, both at the same locations as in Figure 2.

WU ET AL. 8 of 15

21699402, 2023, 4, Downloaded from https://agupubs.onlinelibrary.wiley.com/doi/10.1029/2023JA031354 by Xian Lu, Wiley Online Library on [03/05/2023]. See the Terms and Conditions (https://onlinelibrary.wiley.

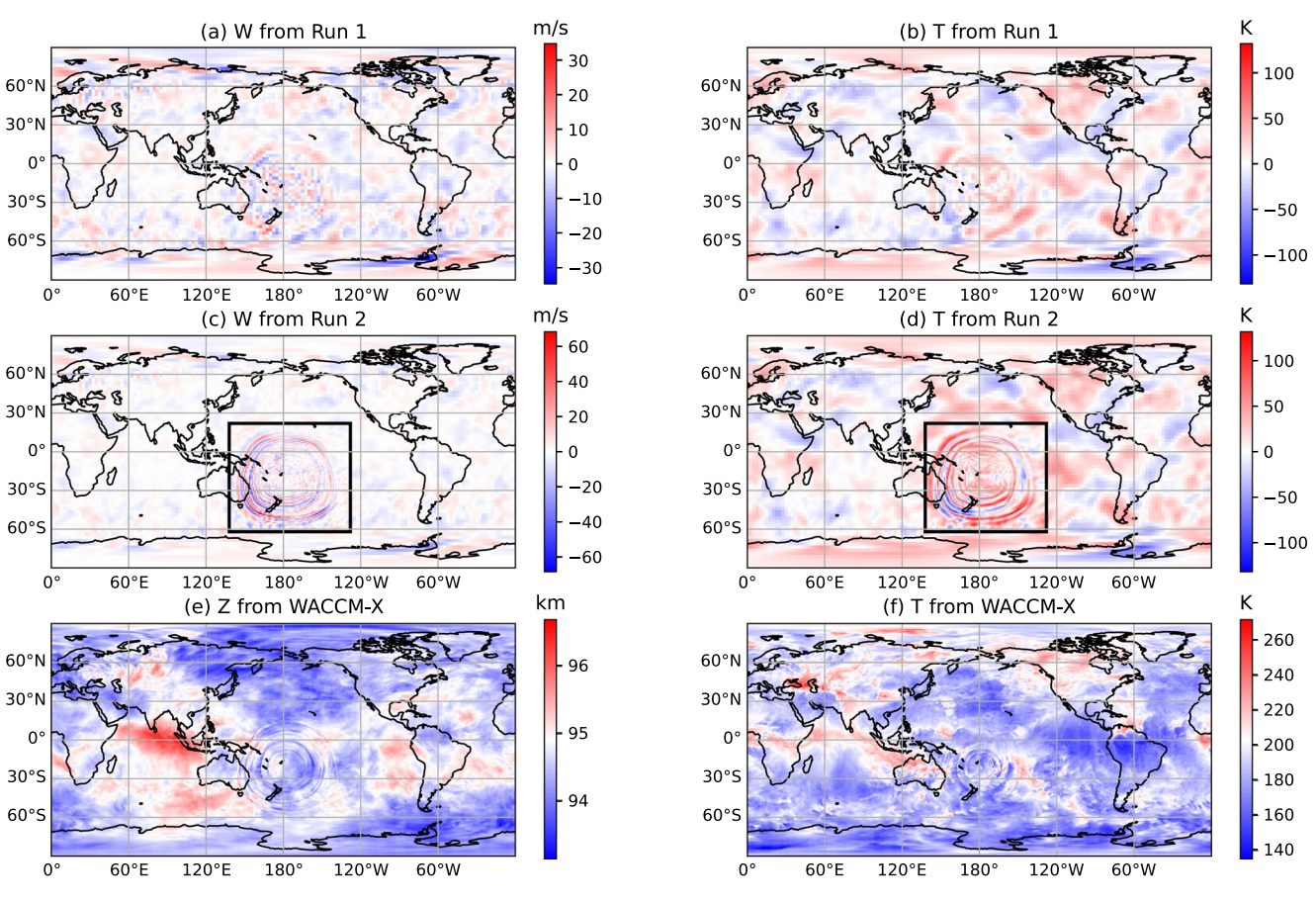


Figure 4. (a–d) Horizontal cross sections of vertical wind and temperature perturbations at z = 2 (~320 km), 08:00 UT in (a, b) Runs 1 and (c, d) 2. (c, d) Are from Run 2g overlaid by Run 2n inside the boxed region. (e, f) WACCM-X geopotential height and temperature extracted at thermosphere-ionosphere-electrodynamics general circulation model lower boundary (z = -7), these two are not the perturbation fields.

3.2. Model Sensitivity to Nudging Fields

To examine the capability of incorporating waves from below at the TIEGCM-NG lower boundary by nudging different wave fields, the model runs belonging to the second testing group in Section 2.2 are performed. Three different runs are performed: Run TUV, indicating T, U, and V are nudged near the lower boundary; Run Z, indicating only Z is nudged; and Run TUVZ, indicating all fields are nudged at the model low pressure levels (Run 2 in Section 3.1).

The vertical and horizontal propagations in the nested domain are shown in Figure 8 for Runs TUV, Z, and TUVZ. Different cross sections are drawn in the figure for different runs including the time-altitude cross section at the epicenter (21°S, 175°W), the time-latitude cross section at z = 2, 175°W, and the longitude-latitude cross section at 08:00 UT, z = 2. Although the vertical and horizontal structures of the GW are similar comparing Figures 8a and 8g (Figures 8b and 8h, 8c and 8i), the magnitude is significantly smaller in Run TUV than in Run TUVZ, 40 m/s versus 100 m/s. On the other hand, comparing Runs Z and TUVZ, no distinguishable differences are identified from Figures 8d and 8g (Figures 8e and 8h, 8f and 8i). The comparison indicates that Z is the most important field to be nudged in GW propagation. In other words, high-frequency GW is most sensitive to Z. The possible reason for this sensitivity can be summarized in two points. First, in this study, high-frequency waves have larger amplitudes and dominate the region of interest. The vertical wind spectrum is sensitive to high-frequency waves, while zonal and meridional wind spectra are sensitive to low-frequency waves (Geller & Gong, 2010). This leads to the dominant high-frequency waves in vertical winds. Second, the vertical wind is proportional to the displacement of Z, but nudging T, U, and V only helps improve the vertical gradient of vertical winds under hydrostatic conditions. So nudging Z directly improves the vertical wind and supports high-frequency waves.

WU ET AL. 9 of 15

21699402, 2023, 4, Downloaded from https://agupubs.onlinelibrary.wiley.com/doi/10.1029/2023/A031354 by Xian Lu, Wiley Online Library on [03/05/2023]. See the Terms and Conditions (https://onlinelibrary.wiley.com/terms

and-conditions) on Wiley Online Library for rules of use; OA articles are governed by the applicable Creative

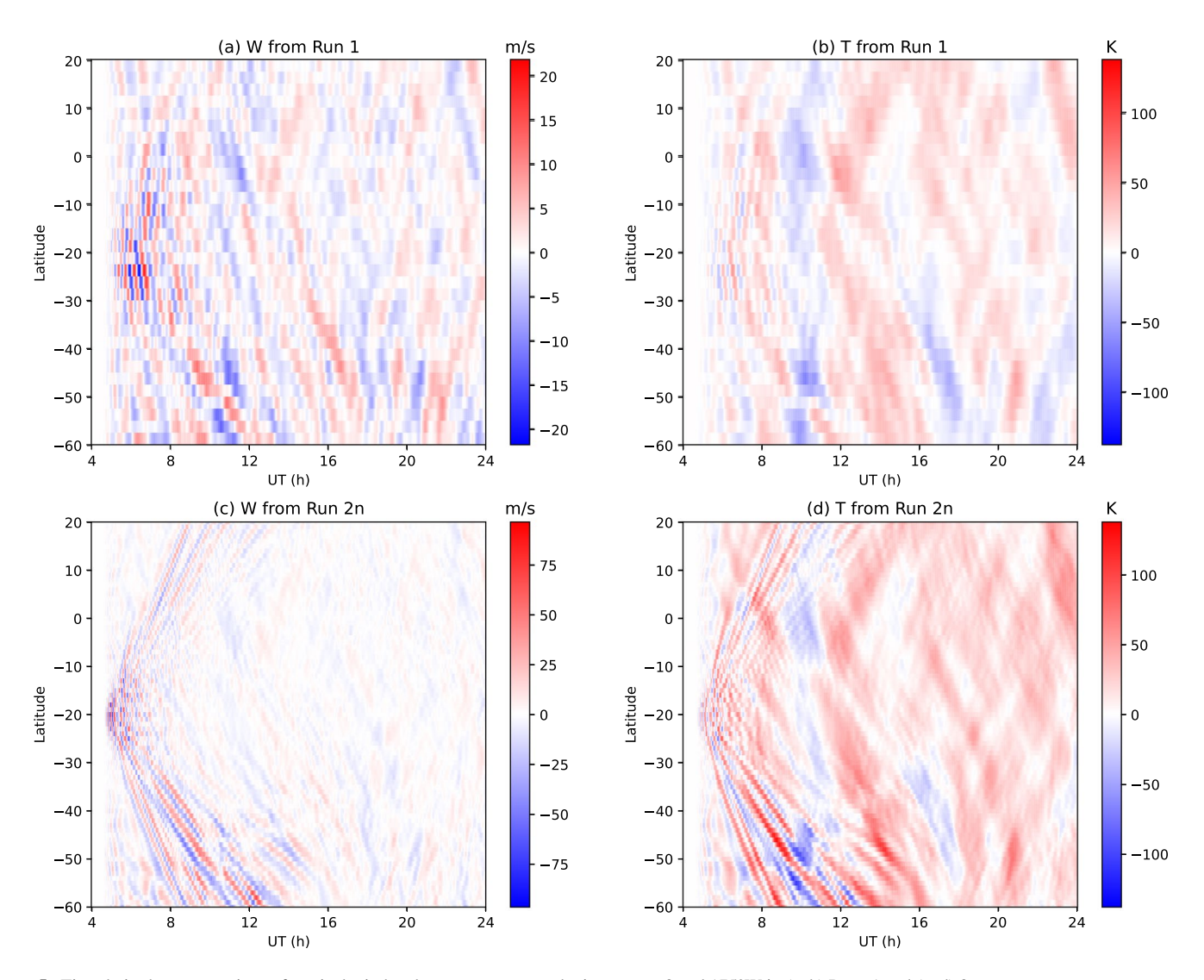


Figure 5. Time-latitude cross sections of vertical wind and temperature perturbations at z = 2 and 175° W in (a, b) Runs 1 and (c, d) 2n.

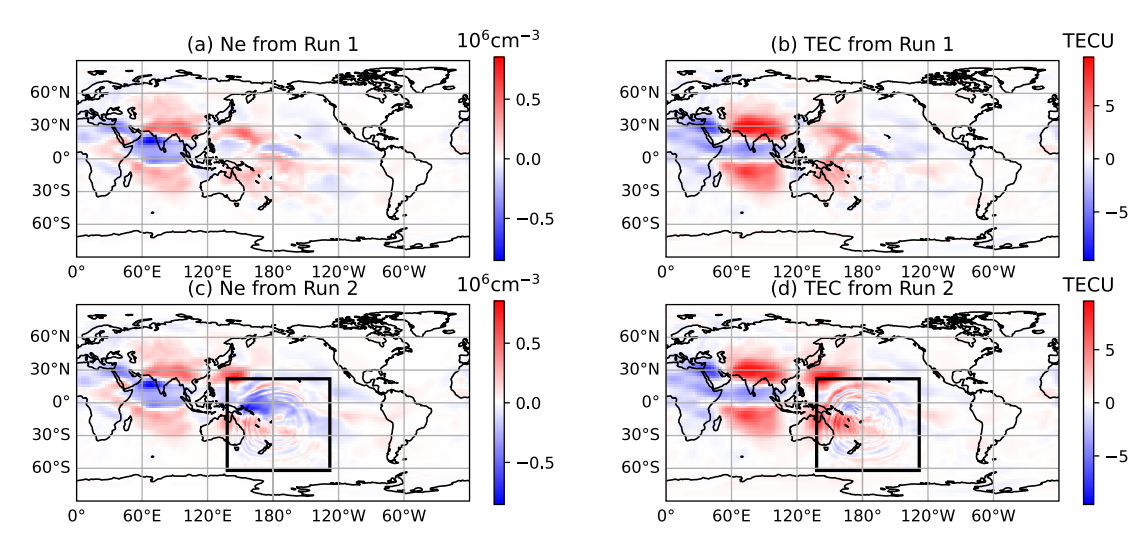


Figure 6. Horizontal cross sections of electron density perturbations at z = 2 and total electron content perturbations at 08:00 UT in (a, b) Runs 1 and (c, d) 2.

WU ET AL. 10 of 15

21699402, 2023, 4, Downloaded from https://agupubs.onlinelibrary.wiley.com/doi/10.1029/2023JA031354 by Xian Lu, Wiley Online Library on [03/05/2023]. See the Terms and Conditions (https://onlinelibrary.wiley.com/

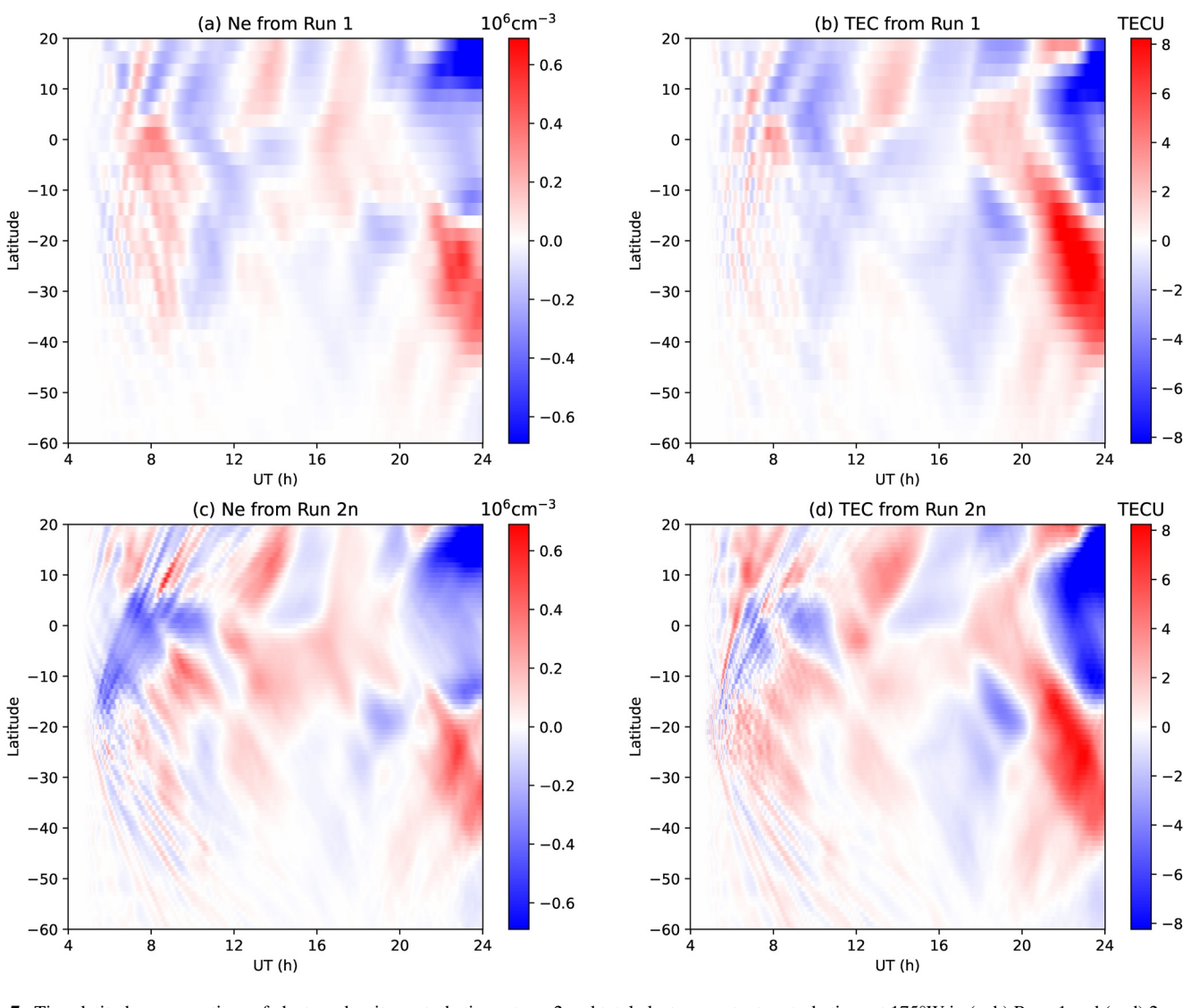


Figure 7. Time-latitude cross sections of electron density perturbations at z = 2 and total electron content perturbations at 175° W in (a, b) Runs 1 and (c, d) 2n.

4. Conclusion and Discussion

We develop a new TIEGCM-NG model which is a regional high-resolution extension of the original TIEGCM to study I-T processes in regional scales. It solves the same set of equations as the original TIEGCM and uses time dependent Dirichlet lateral boundary conditions obtained from the global low-resolution run. Near the nested grid boundaries, the original 4-point stencil in the horizontal finite difference is substituted by a 2-point stencil. The sub-cycling in time largely guarantees the stability of the model in the nested grid domain. We further add the capability of nudging the model at low pressure levels to better simulate the propagation of GWs from the lower atmosphere.

We then nudge WACCM-X simulation results to subscribe GWs into TIEGCM-NG to the impacts of 15 January 2022 volcano eruption at Hunga Tonga-Hunga Ha'apai on the ionospheres via the vertical coupling of GWs. The TIEGCM-NG simulations indicate that high-resolution is critical to simulate the wave propagation. The wave period shifts from long periods to short periods as it propagates from low to high altitudes likely due to the filtering effect of background winds. The wave can further propagate to the ionosphere and lead to significant ionospheric disturbances such as large electron density perturbations. The TIEGCM-NG simulated eruption-induced ionospheric perturbations have a similar magnitude to the observations. The speeds of TAD and TID at ~320 km are estimated to be 300 m/s, in accordance with those derived from the TEC observations. In addition, we perform

WU ET AL. 11 of 15

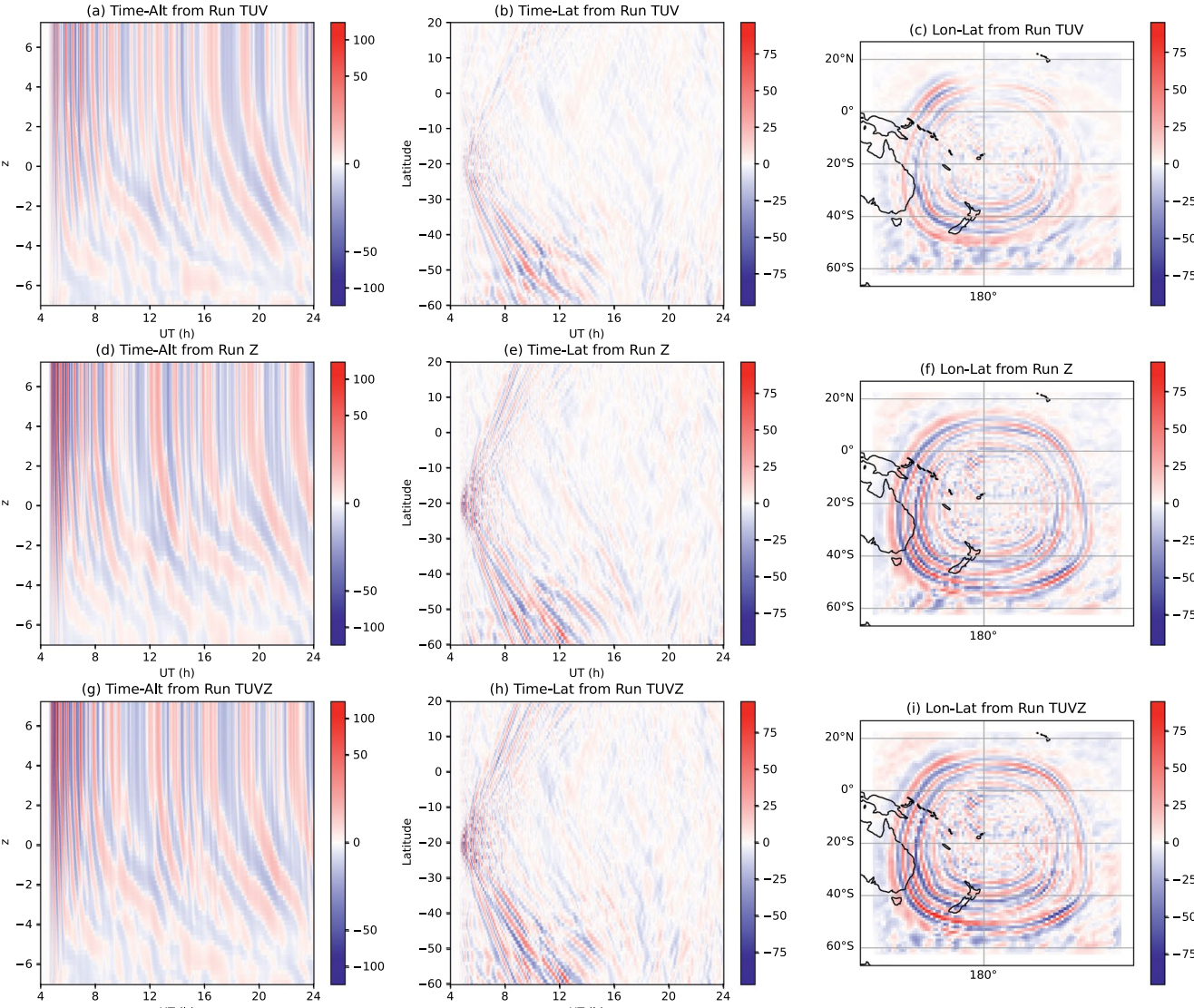


Figure 8. Different cross sections of vertical wind perturbations in Runs (a–c) TUV, (d–f) Z, and (g–i) TUVZ. Time-altitude cross sections at 21°S, 175°W are shown in panels (a, d, and g); time-latitude cross sections at z = 2, 175°W are shown in (b, e, and h); longitude-latitude cross sections at 08:00 UT, z = 2 are shown in panels (c, f, and i). All units are m/s.

a sensitivity test to determine the most important nudging fields to fuse in GWs at the lower boundary. The test shows that geopotential height is the most essential field to be nudged into TIEGCM-NG and geopotential height variations are the easiest to propagate through the I-T system.

However, it is necessary to point out that the simulated GW in this study only covers the one excited by the initial pulse of the volcano eruption. Due to a large amount of water vapor emitted into a very deep column throughout the stratosphere, the release of latent heat at later times also contributes to the excitation of GWs in the real atmosphere. The secondary GW excited by such a mechanism needs to be studied.

It is worthwhile to emphasize that the computation efficiency is much higher in TIEGCM-NG than global high-resolution TIEGCM. Thus TIEGCM-NG can be an ideal choice in applications where computing time is a key factor like near-real-time forecasting on regional scales.

One advantage of TIEGCM-NG compared to local models is that the nested region's background atmosphere (winds, temperatures, etc.) can be more interactive and realistic, representing the time dependence on different external conditions. For example, TIEGCM-NG can assist in investigating under what conditions GWs

WU ET AL. 12 of 15

21699402, 2023, 4, Downloaded from https:

elibrary.wiley.com/doi/10.1029/2023JA031354 by Xian Lu, Wiley Online Library on [03/05/2023]. See

13 of 15

can survive after long-distance propagations and impact the ionosphere (e.g., in the form of TID). Although high-resolution WACCM-X is involved in this study, it is necessary to mention that TIEGCM-NG is not tied to global high-resolution simulations. The purpose of subscribing external field from WACCM-X is to provide GW seeding near the lower boundary. The choice of GW seeding can vary from comprehensive physical models like MAGIC (Heale et al., 2022; Inchin et al., 2022) or theoretical GW models to point-like sources in the lower atmosphere. The computation-efficient nature of TIEGCM-NG is only partially appreciated in the current coupled WACCM-X/TIEGCM-NG study due to the high cost of high-resolution WACCM-X simulations. However, TIEGCM-NG will most likely find its advantage in real applications by coupling to other regional high-resolution models like MAGIC. MAGIC can simulate small-scale GWs while saving computing time (compared to global models) by focusing on a regional area. While MAGIC itself cannot simulate the change of the lateral boundary, a coupled MAGIC/TIEGCM-NG in the future will likely bring new insight into the GW simulation by combining the advantages of global models (no lateral boundaries) and regional models (high resolution).

It is also arguable that a time dependent boundary flux (Neumann condition) instead of the field itself (Dirichlet condition) might better serve the wave propagation across the boundary, but as a starting point and for easy implementation, the field itself is prescribed as the lateral boundary condition in the current development. Among all simulations we perform, there are no significant boundary distortions or reflections and thus we stay with the choice of using a Dirichlet condition. In the current design of the nested grid extension, it is a separate module of the original TIEGCM subroutines, which makes it convenient to modify the physics in the nested grid domain in the future. It is possible to incorporate different sets of physical equations (such as the equations describing the non-hydrostatic processes) in the nested domain and then combine them into global TIEGCM simulations. In this way, even localized high frequency compressible atmospheric waves can be simulated in the framework of TIEGCM. Further extensions of TIEGCM-NG are left as a future task in the study of different atmospheric processes.

Data Availability Statement

The data used to produce the figures in this paper are published at https://data.mendeley.com/datasets/33bbncb5h4.

References

Aa, E., Zhang, S.-R., Erickson, P. J., Vierinen, J., Coster, A. J., Goncharenko, L. P., et al. (2022). Significant ionospheric hole and equatorial plasma bubbles after the 2022 Tonga volcano eruption. Space Weather, 20(7), e2022SW003101. https://doi.org/10.1029/2022SW003101

Alexander, M. J., Geller, M., McLandress, C., Polavarapu, S., Preusse, P., Sassi, F., et al. (2010). Recent developments in gravity-wave effects in climate models and the global distribution of gravity-wave momentum flux from observations and models. *Quarterly Journal of the Royal Meteorological Society*, 136(650), 1103–1124. https://doi.org/10.1002/qj.637

Amores, A., Monserrat, S., Marcos, M., Argüeso, D., Villalonga, J., Jordà, G., & Gomis, D. (2022). Numerical simulation of atmospheric Lamb waves generated by the 2022 Hunga-Tonga volcanic eruption. *Geophysical Research Letters*, 49(6), e2022GL098240. https://doi.org/10.1029/2022GL098240

Carr, J. L., Horváth, Á., Wu, D. L., & Friberg, M. D. (2022). Stereo plume height and motion retrievals for the record-setting Hunga Tonga-Hunga Ha'apai eruption of 15 January 2022. *Geophysical Research Letters*, 49(9), e2022GL098131. https://doi.org/10.1029/2022GL098131

Ern, M., Hoffmann, L., Rhode, S., & Preusse, P. (2022). The mesoscale gravity wave response to the 2022 Tonga volcanic eruption: AIRS and MLS satellite observations and source backtracing. *Geophysical Research Letters*, 49(10), e2022GL098626. https://doi.org/10.1029/2022GL098626 Fritts, D. C. (1984). Gravity wave saturation in the middle atmosphere: A review of theory and observations. *Reviews of Geophysics*, 22(3), 275–308. https://doi.org/10.1029/RG022i003p00275

Fritts, D. C., & Alexander, M. J. (2003). Gravity wave dynamics and effects in the middle atmosphere. Reviews of Geophysics, 41(1), 1003. https://doi.org/10.1029/2001RG000106

Fritts, D. C., & Lund, T. S. (2011). Gravity wave influences in the thermosphere and ionosphere: Observations and recent modeling. In *Aeronomy*

of the Earth's atmosphere and ionosphere (pp. 109–130). https://doi.org/10.1007/978-94-007-0326-1_8 Fritts, D. C., & Nastrom, G. D. (1992). Sources of mesoscale variability of gravity waves. Part II: Frontal, convective, and jet stream excitation.

Journal of the Atmospheric Sciences, 49(2), 111–127. https://doi.org/10.1175/1520-0469(1992)049<0111:SOMVOG>2.0.CO;2
Gasque, L. C., Wu, Y.-J., Harding, B. J., Immel, T. J., & Triplett, C. C. (2022). Rapid volcanic modification of the E-region dynamo: ICON's first

glimpse of the Tonga eruption. *Geophysical Research Letters*, 49(18), e2022GL100825. https://doi.org/10.1029/2022GL100825 Geller, M. A., & Gong, J. (2010). Gravity wave kinetic, potential, and vertical fluctuation energies as indicators of different frequency gravity

waves. Journal of Geophysical Research, 115(D11), D11111. https://doi.org/10.1029/2009JD012266
Gettelman, A., Mills, M. J., Kinnison, D. E., Garcia, R. R., Smith, A. K., Marsh, D. R., et al. (2019). The whole atmosphere community climate

model version 6 (WACCM6). Journal of Geophysical Research: Atmospheres, 124(23), 12380–12403. https://doi.org/10.1029/2019JD030943 Harding, B. J., Wu, Y.-J. J., Alken, P., Yamazaki, Y., Triplett, C. C., Immel, T. J., et al. (2022). Impacts of the January 2022 Tonga volcanic eruption on the ionospheric dynamo: ICON-MIGHTI and swarm observations of extreme neutral winds and currents. Geophysical Research Letters, 49(9), e2022GL098577. https://doi.org/10.1029/2022GL098577

Heale, C. J., Bossert, K., & Vadas, S. L. (2022). 3D numerical simulation of secondary wave generation from mountain wave breaking over Europe. Journal of Geophysical Research: Atmospheres, 127(5), e2021JD035413. https://doi.org/10.1029/2021JD035413

Acknowledgments

WU ET AL.

We thank Benjamin C. Martinez from Clemson University and Dong Lin from National Center for Atmospheric Research for the internal review of this manuscript. Haonan Wu and Xian Lu are supported by NASA 80NSSC22K0018, NNX17AG10G, 80NSSC22K1010, 80NSSCK19K0810 and NSF AGS-2149695, CAREER-1753214, and AGS-2012994. Wenbin Wang is supported in part by the NSF Grant AGS-203843 and the NASA DRIVE Science Center for Geospace Storms (CGS) under Award 80NSSC22M0163.



Journal of Geophysical Research: Space Physics

- 10.1029/2023JA031354
- Hines, C. O. (1960). Internal atmospheric gravity waves at ionospheric heights. Canadian Journal of Physics, 38(11), 1441–1481. https://doi.org/10.1139/p60-150
- Holton, J. R. (1982). The role of gravity wave induced drag and diffusion in the momentum budget of the mesosphere. *Journal of the Atmospheric Sciences*, 39(4), 791–799. https://doi.org/10.1175/1520-0469(1982)039<0791:TROGWI>2.0.CO:2
- Holton, J. R. (1983). The influence of gravity wave breaking on the general circulation of the middle atmosphere. *Journal of the Atmospheric Sciences*, 40(10), 2497–2507. https://doi.org/10.1175/1520-0469(1983)040<2497:TIOGWB>2.0.CO;2
- Inchin, P. A., Heale, C. J., Snively, J. B., & Zettergren, M. D. (2022). Numerical modeling of tsunami-generated acoustic-gravity waves in mesopause airglow. *Journal of Geophysical Research: Space Physics*, 127(8), e2022JA030301. https://doi.org/10.1029/2022JA030301
- Jones, M., Jr., Drob, D. P., Siskind, D. E., McCormack, J. P., Maute, A., McDonald, S. E., & Dymond, K. F. (2018). Evaluating different techniques for constraining lower atmospheric variability in an upper atmosphere general circulation model: A case study during the 2010 sudden stratospheric warming. *Journal of Advances in Modeling Earth Systems*, 10(12), 3076–3102. https://doi.org/10.1029/2018MS001440
- Klemp, J. B., & Durran, D. R. (1983). An upper boundary condition permitting internal gravity wave radiation in numerical mesoscale models. Monthly Weather Review, 111(3), 430–444. https://doi.org/10.1175/1520-0493(1983)111<0430:AUBCPI>2.0.CO;2
- Lin, J.-T., Rajesh, P. K., Lin, C. C. H., Chou, M.-Y., Liu, J.-Y., Yue, J., et al. (2022). Rapid conjugate appearance of the giant ionospheric Lamb wave signatures in the northern hemisphere after Hunga-Tonga volcano eruptions. *Geophysical Research Letters*, 49(8), e2022GL098222. https://doi.org/10.1029/2022GL098222
- Lindzen, R. S. (1981). Turbulence and stress owing to gravity wave and tidal breakdown. *Journal of Geophysical Research*, 86(C10), 9707–9714. https://doi.org/10.1029/JC086iC10p09707
- Liu, H.-L., Bardeen, C. G., Foster, B. T., Lauritzen, P., Liu, J., Lu, G., et al. (2018). Development and validation of the whole atmosphere community climate model with thermosphere and ionosphere extension (WACCM-X 2.0). *Journal of Advances in Modeling Earth Systems*, 10(2), 381–402, https://doi.org/10.1002/2017MS001232
- Liu, H.-L., Foster, B. T., Hagan, M. E., McInerney, J. M., Maute, A., Qian, L., et al. (2010). Thermosphere extension of the whole atmosphere community climate model. *Journal of Geophysical Research*, 115(A12), A12302. https://doi.org/10.1029/2010JA015586
- Liu, H.-L., Lauritzen, P. H., Vitt, F., & Goldhaber, S. (2022). Thermospheric and ionospheric effects by gravity waves from the lower atmosphere. Earth and Space Science Open Archive. https://doi.org/10.1002/essoar.10511744.1
- Liu, J., Liu, H.-L., Wang, W., Burns, A. G., Wu, Q., Gan, Q., et al. (2018). First results from the ionospheric extension of WACCM-X during the deep solar minimum year of 2008. *Journal of Geophysical Research: Space Physics*, 123(2), 1534–1553. https://doi.org/10.1002/2017JA025010
- Liu, X., Xu, J., Yue, J., & Kogure, M. (2022). Strong gravity waves associated with Tonga volcano eruption revealed by SABER observations. Geophysical Research Letters, 49(10), e2022GL098339. https://doi.org/10.1029/2022GL098339
- Lynett, P., McCann, M., Zhou, Z., Renteria, W., Borrero, J., Greer, D., et al. (2022). Diverse tsunamigenesis triggered by the Hunga Tonga-Hunga Ha'apai eruption. *Nature*, 609(7928), 728–733. https://doi.org/10.1038/s41586-022-05170-6
- Maute, A., Hagan, M. E., Yudin, V., Liu, H.-L., & Yizengaw, E. (2015). Causes of the longitudinal differences in the equatorial vertical E × B drift during the 2013 SSW period as simulated by the TIME-GCM. *Journal of Geophysical Research: Space Physics*, 120(6), 5117–5136. https://doi.org/10.1002/2015JA021126
- McFarlane, N. A. (1987). The effect of orographically excited gravity wave drag on the general circulation of the lower stratosphere and troposphere. *Journal of the Atmospheric Sciences*, 44(14), 1775–1800. https://doi.org/10.1175/1520-0469(1987)044<1775:TEOOEG>2.0.CO;2
- Millán, L., Santee, M. L., Lambert, A., Livesey, N. J., Werner, F., Schwartz, M. J., et al. (2022). The Hunga Tonga-Hunga Ha'apai Hydration of the stratosphere. *Geophysical Research Letters*, 49(13), e2022GL099381. https://doi.org/10.1029/2022GL099381
- Nastrom, G. D., & Fritts, D. C. (1992). Sources of mesoscale variability of gravity waves. Part I: Topographic excitation. *Journal of the Atmospheric Sciences*, 49(2), 101–110. https://doi.org/10.1175/1520-0469(1992)049<0101:SOMVOG>2.0.CO;2
- Omira, R., Ramalho, R. S., Kim, J., González, P. J., Kadri, U., Miranda, J. M., et al. (2022). Global Tonga tsunami explained by a fast-moving atmospheric source. *Nature*, 609(7928), 734–740. https://doi.org/10.1038/s41586-022-04926-4
- Palmer, T. N., Shutts, G. J., & Swinbank, R. (1986). Alleviation of a systematic westerly bias in general circulation and numerical weather prediction models through an orographic gravity wave drag parametrization. *Quarterly Journal of the Royal Meteorological Society*, 112(474), 1001–1039. https://doi.org/10.1002/qj.49711247406
- Qian, L., Burns, A. G., Emery, B. A., Foster, B., Lu, G., Maute, A., et al. (2014). The NCAR TIE-GCM: A community model of the coupled thermosphere/ionosphere system. In *Modeling the ionosphere-thermosphere system* (pp. 73–83). https://doi.org/10.1002/9781118704417.ch7
- Richmond, A. D., Ridley, E. C., & Roble, R. G. (1992). A thermosphere/ionosphere general circulation model with coupled electrodynamics. Geophysical Research Letters, 19(6), 601–604. https://doi.org/10.1029/92GL00401
- Roble, R. G., Ridley, E. C., Richmond, A. D., & Dickinson, R. E. (1988). A coupled thermosphere/ionosphere general circulation model. Geophysical Research Letters, 15(12), 1325–1328. https://doi.org/10.1029/GL015i012p01325
- Schnepf, N. R., Minami, T., Toh, H., & Nair, M. C. (2022). Magnetic signatures of the 15 January 2022 Hunga Tonga–Hunga Ha'apai volcanic eruption. Geophysical Research Letters, 49(10), e2022GL098454. https://doi.org/10.1029/2022GL098454
- Themens, D. R., Watson, C., Žagar, N., Vasylkevych, S., Elvidge, S., McCaffrey, A., et al. (2022). Global propagation of ionospheric disturbances associated with the 2022 Tonga volcanic eruption. *Geophysical Research Letters*, 49(7), e2022GL098158. https://doi.org/10.1029/2022GL098158
- Vadas, S. L., & Fritts, D. C. (2005). Thermospheric responses to gravity waves: Influences of increasing viscosity and thermal diffusivity. *Journal of Geophysical Research*, 110(D15), D15103. https://doi.org/10.1029/2004JD005574
- Vadas, S. L., & Liu, H.-L. (2009). Generation of large-scale gravity waves and neutral winds in the thermosphere from the dissipation of convectively generated gravity waves. *Journal of Geophysical Research*, 114(A10), A10310. https://doi.org/10.1029/2009JA014108
- Van Eyken, A. P., Williams, P. J. S., Maude, A. D., & Morgan, G. (1982). Atmospheric gravity waves and sporadic-E. *Journal of Atmospheric and Terrestrial Physics*, 44(1), 25–29. https://doi.org/10.1016/0021-9169(82)90089-7
- Wang, W., Killeen, T. L., Burns, A. G., & Roble, R. G. (1999). A high-resolution, three-dimensional, time dependent, nested grid model of the coupled thermosphere-ionosphere. *Journal of Atmospheric and Solar-Terrestrial Physics*, 61(5), 385–397. https://doi.org/10.1016/ \$1364-6826(98)00079-0
- Wright, C. J., Hindley, N. P., Alexander, M. J., Barlow, M., Hoffmann, L., Mitchell, C. N., et al. (2022). Surface-to-space atmospheric waves from Hunga Tonga–Hunga Ha'apai eruption. *Nature*, 609(7928), 741–746. https://doi.org/10.1038/s41586-022-05012-5
- Yamazaki, Y., Soares, G., & Matzka, J. (2022). Geomagnetic detection of the atmospheric acoustic resonance at 3.8 mHz during the Hunga Tonga eruption event on 15 January 2022. *Journal of Geophysical Research: Space Physics*, 127(7), e2022JA030540. https://doi.org/10.1029/2022JA030540
- Zhang, J., Xu, J., Wang, W., Wang, G., Ruohoniemi, J. M., Shinbori, A., et al. (2022). Oscillations of the ionosphere caused by the 2022 Tonga volcanic eruption observed with SuperDARN radars. Geophysical Research Letters, 49(20), e2022GL100555. https://doi. org/10.1029/2022GL100555

WU ET AL. 14 of 15



Journal of Geophysical Research: Space Physics

10.1029/2023JA031354

Zhang, S.-R., Vierinen, J., Aa, E., Goncharenko, L. P., Erickson, P. J., Rideout, W., et al. (2022). 2022 Tonga volcanic eruption induced global propagation of ionospheric disturbances via Lamb waves. Frontiers in Astronomy and Space Sciences, 9. https://doi.org/10.3389/ fspas.2022.871275

Zhu, Y., Bardeen, C. G., Tilmes, S., Mills, M. J., Wang, X., Harvey, V. L., et al. (2022). Perturbations in stratospheric aerosol evolution due to the water-rich plume of the 2022 Hunga-Tonga eruption. *Communications Earth and Environment*, 3(1), 248. https://doi.org/10.1038/s43247.022-00580.w

WU ET AL. 15 of 15